J. Fluid Mech. (2008), *vol.* 607, *pp.* 25–49. © 2008 Cambridge University Press
doi:10.1017/S0022112008001742 Printed in the United Kingdom

Near-inertial parametric subharmonic instability

W. R. YOUNG[1], Y.-K. TSANG[1] AND N. J. BALMFORTH[2]

[1]Scripps Institution of Oceanography, University of California, San Diego, CA 92093-0230, USA

[2]Departments of Mathematics and Earth & Ocean Science, University of British Columbia, Vancouver, Canada

(Received 25 May 2007 and in revised form 11 March 2008)

New analytic estimates of the rate at which parametric subharmonic instability (PSI) transfers energy to high-vertical-wavenumber near-inertial oscillations are presented. These results are obtained by a heuristic argument which provides insight into the physical mechanism of PSI, and also by a systematic application of the method of multiple time scales to the Boussinesq equations linearized about a 'pump wave' whose frequency is close to twice the inertial frequency. The multiple-scale approach yields an amplitude equation describing how the $2f_0$-pump energizes a vertical continuum of near-inertial oscillations. The amplitude equation is solved using two models for the $2f_0$-pump: (i) an infinite plane internal wave in a medium with uniform buoyancy frequency; (ii) a vertical mode one internal tidal wavetrain in a realistically stratified and bounded ocean. In case (i) analytic expressions for the growth rate of PSI are obtained and validated by a successful comparison with numerical solutions of the full Boussinesq equations. In case (ii), numerical solutions of the amplitude equation indicate that the near-inertial disturbances generated by PSI are concentrated below the base of the mixed layer where the velocity of the pump wave train is largest. Based on these examples we conclude that the *e*-folding time of PSI in oceanic conditions is of the order of ten days or less.

1. Introduction

Mixing a stably stratified ocean by breaking internal gravity waves requires the transfer of energy from the low vertical modes excited by wind and tides to near-inertial waves with small vertical scale. Hibiya, Nagasawa & Niwa (2002) and MacKinnon & Winters (2005, 2008) have discovered an important route for this transfer: at the specific latitude 28.8°, where the M_2 tidal frequency is equal to twice the local inertial frequency, a northward propagating M_2 internal tide, with mode one vertical structure, rapidly transfers energy to the near-inertial subharmonic via parametric subharmonic instability (PSI). The near-inertial wave at the critical latitude 28.8°N has small vertical scale and large shear so that overturning and mixing is indicated. Earlier work by Nagasawa, Niwa & Hibiya (2000) argues that near-inertial waves generated by mid-latitude storms in the North Pacific propagate towards the equator until their frequency is equal to twice the local inertial frequency. At this point, PSI rapidly transfers energy to half-frequency near-inertial waves with much smaller vertical scale. Figure 1 shows PSI and the excitation of small vertical scales using a numerical solution of the two-dimensional Boussinesq equations.

Using a global tidal model, Simmons (2008) shows a web of filamentary M_2 internal wave beams radiating from topographic wavemakers. The $M_2/2$ subharmonic is generated when beams cross the critical latitude, resulting in an accumulation of near-inertial energy and shear at 28.8°. In another numerical study, Gerkema, Staquet &

https://doi.org/10.1017/S0022112008001742 Published online by Cambridge University Press

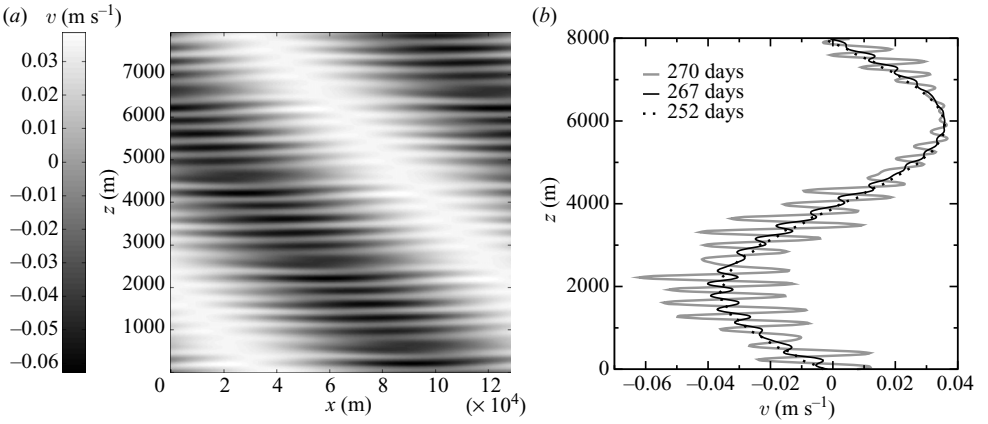


FIGURE 1. A solution of the two-dimensional Boussinesq equations obtained using the streamfunction-vorticity formulation and a pseudospectral code. The initial condition is an infinite plane wave, as in (4.1), plus very small random noise. The wavenumbers are $k = 2\pi/(129 \times 10^3\text{m})$ and $m = 2\pi/(8 \times 10^3\text{m})$, corresponding to the gravest length scales of the computational domain. The wave amplitude is $a = 0.1551\,\text{m}^2\,\text{s}^{-2}$ so that the wave has a root-mean-square horizontal velocity of $5.65\,\text{cm}\,\text{s}^{-1}$. The Coriolis frequency $f_0 = 7.04 \times 10^{-5}\,\text{s}^{-1}$, corresponds to 28.8° North, $\omega = M_2 = 2f_0$ and $N = 28\,f_0$. (*a*) A snapshot of the meridional velocity $v(x, z, t)$ at $t = 270$ days. (*b*) Vertical profiles of v; in the profile at $t = 252$ days, the small noise is not yet evident. In the later two profiles, PSI has amplified the noise into a near-inertial oscillation with relatively small vertical scale.

Bouruet-Aubertot (2006) show that M_2 tidal beams generated at the shelf-break are subject to PSI which generates near-inertial disturbances along the beam: PSI is so rapid that there is considerable energy transfer to $M_2/2$ even before the first bottom bounce.

These recent works force a revision of results concerning nonlinear interactions between oceanic internal gravity waves and the role of PSI in moving energy to near-inertial waves of small vertical scale. In particular, Olbers & Pomphrey's (1981) conclusion that the 'spreading of tidal energy across the internal wave continuum by resonant coupling... is irrelevant for the energy balance' must be reassessed. This is symptomatic of a larger issue: there is uncertainty about nonlinear internal wave interaction rates, and this uncertainty is most acute for interactions involving the near-inertial spectral peak (Garrett & St Laurent 2002). Most of the early work on interactions among ocean internal gravity waves summarized by Müller *et al.* (1986) is based on the random phase assumption; this leads to slow interaction rates and inefficient energy transfer.

The numerical studies discussed above indicate that the coherent waves generated by tides and large-scale atmospheric forcing have much faster transfer rates. However, there are significant differences regarding the growth rate of PSI even amongst these investigators: MacKinnon & Winters (2005, 2007) find that the e-folding time is 5 or 10 days in their simulations; Gerkema *et al.* (2006) find a 2 day e-folding time; Simmons (2007) estimates an e-folding time of roughly 15 days. The growth rate of PSI depends on the amplitude and structure of the primary M_2 tidal wave so these disparities might be expected in differently configured simulations. One of our goals here is to provide reliable analytic estimates for the rate at which energy is transferred to the near-inertial spectral peak by the parametric subharmonic instability of a coherent wave with frequency close to $2f_0$.

https://doi.org/10.1017/S0022112008001742 Published online by Cambridge University Press

We emphasize the importance of rotation: much of the previous theoretical and experimental work on PSI has focused on excitation and breaking in the non-rotating case (e.g. Mied 1976; Drazin 1977; Klostermeyer 1991; Bouruet-Aubertot, Sommeria & Staquet 1995; Benielli & Sommeria 1998). Here we are concerned with a particular type of PSI – near-inertial PSI – in which the primary wave has a frequency $\omega \approx 2f_0$, where f_0 is the local inertial frequency, so that the recipient subharmonic is a near-inertial oscillation. In this rotationally dominated situation, the energy transfer is particularly strong because near-inertial oscillations are almost stationary and therefore might dissipate locally forming MacKinnon & Winters's 'subtropical catastrophe'.

In § 2, we show that for near-inertial PSI there is a simple fluid-mechanical solution which is more informative than the pendulum analogy. In § 3, we extend and develop the formalism of Young & Ben Jelloul (1997) to obtain a general description of the excitation of near-inertial waves by PSI. In § 4, we use the amplitude equation from § 3 to analyse the stability of an infinite-plane internal gravity wave. This analysis provides analytic expressions for the growth rate of PSI. The reduced description of § 3 is validated by a successful comparison of the analytic growth rate with numerical solutions of the Boussinesq equations. In § 5, we consider the parametric instability of a vertical mode one, tidal wavetrain in a realistically stratified ocean. In § 6, we discuss the main results of this paper, emphasizing that PSI does not select a preferred vertical scale.

2. The physical basis of near-inertial PSI

PSI is one of the three classes of resonant interactions identified by McComas & Bretherton (1977) as dominating energy transfer rates between internal gravity waves under rapidly rotating conditions in the ocean. In the original conception of McComas & Bretherton, PSI transfers energy from low wavenumbers with frequency ω to high wavenumbers with frequency $\omega/2$. Transfer to the subharmonic $\omega/2$ is reminiscent of the response of a pendulum with a vertically oscillated support, and this mechanical analogy is often the basis of a physical explanation of PSI (e.g. as in Benielli & Sommeria 1998). However, in the special case of PSI with $\omega \approx 2f_0$ there is an alternative and more informative fluid mechanical explanation. Thus as a motivating preamble to the more general discussion in § 3, we first consider an idealized limit in which (U, V) denotes the horizontal velocity of the background flow where, following Weller (1982),

$$\begin{pmatrix} U \\ V \end{pmatrix} = \begin{pmatrix} U_x & U_y \\ V_x & V_y \end{pmatrix} \begin{pmatrix} x \\ y \end{pmatrix}. \tag{2.1}$$

The entries of the 2×2 matrix above are functions of depth z and time t and incompressibility demands that the vertical velocity $W(z, t)$ is given by $U_x + V_y + W_z = 0$.

Now we consider how the background flow (U, V, W) interacts with a *pure inertial oscillation*. By a pure inertial oscillation we mean a disturbance with infinite spatial scale in the horizontal so that the velocity is $[u(z, t), v(z, t), 0]$. A pure inertial oscillation has no pressure or buoyancy signal and thus the dynamics are entirely governed by the horizontal momentum equations:

$$\left.\begin{aligned} u_t + Wu_z + uU_x + vU_y - f_0 v = 0, \\ v_t + Wv_z + uV_x + vV_y + f_0 u = 0. \end{aligned}\right\} \tag{2.2}$$

https://doi.org/10.1017/S0022112008001742 Published online by Cambridge University Press

The energy equation obtained from (2.2) is

$$e_t + We_z - W_z e + \tfrac{1}{2}(u^2 - v^2)(U_x - V_y) + uv(U_y + V_x) = 0, \tag{2.3}$$

where $e \equiv (u^2 + v^2)/2$ is the energy density of the inertial oscillation.

For a pure inertial oscillation, the quantities $u^2 - v^2$ and uv prominently contain the second harmonics $\exp(\pm 2\mathrm{i} f_0 t)$, while $e = (u^2 + v^2)/2$ contains only the zero frequency. Thus, from (2.3), we can anticipate the existence of parametric subharmonic instability provided that the background strain rates $U_x - V_y$ and $U_y + V_x$ also contain the $2f_0$-harmonic. Then the combinations $(u^2 - v^2)(U_x - V_y)/2$ and $uv(U_y + V_x)$ can reinforce the zero-frequency in e. We refer to this as '$2f_0$-pumping'.

Because e contains only the zero frequency, the spectral content of W at $2f_0$ does not lead to instability via We_z and $W_z e$ in (2.3). Instead, a zero-frequency component in W might result in instability via We_z and $W_z e$. However, we assume that the low-frequency part of the background flow is in geostrophic balance and consequently there is no zero-frequency spectral content in W.

The growth rate of the instability can be calculated with a simple averaging argument as detailed shortly. The main deduction from (2.3) is that energy transfer to the near-inertial peak is associated with the spectral content of the strain rates $U_x - V_y$ and $U_y + V_x$ at $2f_0$. Neither the vertical vorticity nor the horizontal divergence of the background flow are decisive. Vertical straining via W_z is not the essential physical mechanism of near-inertial PSI: the instability is driven by $2f_0$-pumping.

To quantify this further, it is convenient to first rewrite (2.2) exactly in terms of the 'back-rotated' velocity $\mathcal{Q}(t, z) \equiv \exp(\mathrm{i} f_0 t)(u + \mathrm{i}v)$ as

$$\mathcal{Q}_t + W\mathcal{Q}_z + \tfrac{1}{2}[(U_x + V_y) + \mathrm{i}(V_x - U_y)]\mathcal{Q} + \tfrac{1}{2}[(U_x - V_y) + \mathrm{i}(V_x + U_y)]\mathrm{e}^{2\mathrm{i}f_0 t}\mathcal{Q}^* = 0. \tag{2.4}$$

We assume that the background flow and the near-inertial oscillation interact weakly so that the envelope $\mathcal{Q}(z, t)$ is evolving slowly relative to the inertial time scale. The secular evolution of $\mathcal{Q}(z, t)$ is then obtained by time-averaging (denoted by an overbar) (2.4) over an interval which is long relative to f_0^{-1}:

$$\bar{\mathcal{Q}}_t + \tfrac{1}{2}\mathrm{i}\zeta\bar{\mathcal{Q}} + \tfrac{1}{2}\Upsilon\bar{\mathcal{Q}}^* = 0, \tag{2.5}$$

where

$$\zeta \equiv \bar{V}_x - \bar{U}_y, \tag{2.6}$$

is the vertical vorticity of the low-frequency part of the background flow. (In passing from (2.4) to (2.5) we assume that the low-frequency part of the background flow is geostrophically balanced so that $\bar{W} = \bar{U}_x + \bar{V}_y = 0$.) The term involving $\mathrm{i}\zeta/2$ in (2.5) is Kunze's (1985) result that the effective inertial frequency is shifted away from the local inertial frequency by half of the relative vorticity of the low-frequency geostrophic background flow – see also Klein & Llewellyn Smith (2001) and Klein, Llewellyn Smith & Lapeyre (2004). The other coefficient in (2.5) is the amplitude of the $2f_0$-pump:

$$\Upsilon \equiv \overline{[(U_x - V_y) + \mathrm{i}(V_x + U_y)]\mathrm{e}^{2\mathrm{i}f_0 t}}, \tag{2.7}$$

which is non-zero if the background strain rates have spectral content at $2f_0$.

To illustrate this transfer of energy, suppose that ζ is constant and that the background flow in (2.7) contains the frequencies $\pm(2f_0 + \sigma)$, where $\sigma \ll 2f_0$ is a small de-tuning of the resonance. In this case $\Upsilon = \Upsilon_0 \exp(-\mathrm{i}\sigma t)$. The solution of (2.5)

https://doi.org/10.1017/S0022112008001742 Published online by Cambridge University Press

has the form

$$\bar{\mathscr{Q}} = \mathrm{e}^{-\mathrm{i}\sigma t/2}\left(A_1\mathrm{e}^{st} + A_2^*\mathrm{e}^{s^*t}\right), \tag{2.8}$$

where

$$s^2 = \tfrac{1}{4}|\Upsilon_0|^2 - \tfrac{1}{4}(\zeta - \sigma)^2\,. \tag{2.9}$$

The strength of the $2f_0$-pump exceeds de-tuning if $|\Upsilon_0| > |\zeta - \sigma|$ and then s is real so that the energy of the inertial oscillation grows exponentially via PSI. The expression for the growth rate s in (2.9) points to an interesting competition between Kunze's frequency shift $\zeta/2$, the de-tuning σ and the pump strength $|\Upsilon_0|$.

3. A general framework for near-inertial PSI

In § 2, we considered an idealized limit in which the background flow has a very large scale as in (2.1), and the near-inertial oscillation has an even larger horizontal scale. We now lift these assumptions regarding the idealized spatial structure of the solution and develop a general framework describing the evolution of near-inertial oscillations. Young & Ben Jelloul (1997) considered the propagation of near-inertial oscillations through a geostrophic flow which changes slowly relative to the inertial period. Our strategy is to extend the multiple time-scale approach of Young & Ben Jelloul by considering a background flow consisting of both a geostrophic component and a $2f_0$-pump flow. Young & Ben Jelloul show that there is no transfer of energy between the geostrophic part of the background flow and the near-inertial waves. This result has been confirmed via higher-order asymptotics by Reznik, Zeitlin & Ben Jelloul (2001). Thus the $2f_0$-pump component of the background plays the essential role of energizing the near-inertial oscillations via the mechanism of § 2.

We use the β-plane approximation pivoted around f_0:

$$f = f_0 + \beta y. \tag{3.1}$$

As in § 2, we use (U, V, W, B, P) to denote the velocity, buoyancy and pressure of the background flow. With (u, v, w, b, p) we denote the fields associated with the near-inertial oscillation. Thus, for example, the total density field has the form

$$\rho = \rho_0\left[1 - g^{-1}\int_0^z N^2(z')\,\mathrm{d}z' - g^{-1}B - g^{-1}b\right], \tag{3.2}$$

where $N^2(z)$ is the buoyancy frequency and the background buoyancy is

$$B(\boldsymbol{x}, t) = B_g(\boldsymbol{x}, t) + B_p(\boldsymbol{x}, t). \tag{3.3}$$

In (3.3), B_g is the buoyancy of the geostrophic flow and the pump buoyancy B_p is

$$B_p(\boldsymbol{x}, t) = \tilde{B}_p^*(\boldsymbol{x}, t)\mathrm{e}^{2\mathrm{i}f_0t} + \tilde{B}_p(\boldsymbol{x}, t)\mathrm{e}^{-2\mathrm{i}f_0t}. \tag{3.4}$$

The envelope $\tilde{B}_p$ evolves on the slow time scale, i.e. the carrier $\exp(\pm 2\mathrm{i}f_0t)$ in (3.4) contains the dominant frequency $2f_0$. There is an analogous decomposition (geostrophic, g, plus pump, p) for the other background fields. The geostrophic component can be derived from a streamfunction, $\psi = P_g/f_0$, via

$$(U_g, V_g, W_g, B_g) = (-\psi_y, \psi_x, 0, f_0\psi_z). \tag{3.5}$$

Thus, for example, the background zonal velocity is

$$U = -\psi_y + \tilde{U}_p^*\mathrm{e}^{2\mathrm{i}f_0t} + \tilde{U}_p\mathrm{e}^{-2\mathrm{i}f_0t}. \tag{3.6}$$

https://doi.org/10.1017/S0022112008001742 Published online by Cambridge University Press

Because the geostrophic vertical velocity is zero, $W(\boldsymbol{x}, t)$ consists solely of the pump component:

$$W = \tilde{W}_p^* e^{2if_0 t} + \tilde{W}_p e^{-2if_0 t}. \tag{3.7}$$

Linearizing the Boussinesq equations around the background we obtain:

$$u_t + Uu_x + Vu_y + Wu_z + uU_x + vU_y + wU_z - fv + p_x = 0, \tag{3.8}$$

$$v_t + Uv_x + Vv_y + Wv_z + uV_x + vV_y + wV_z + fu + p_y = 0, \tag{3.9}$$

$$-b + p_z = 0, \tag{3.10}$$

$$u_x + v_y + w_z = 0, \tag{3.11}$$

$$b_t + Ub_x + Vb_y + Wb_z + uB_x + vB_y + wB_z + wN^2 = 0. \tag{3.12}$$

We emphasize that the PSI is driven solely and essentially by the pump component of the background flow, e.g. U_p in (3.6). The geostrophic component, which is derived from ψ, is included to make contact with the earlier results in Young & Ben Jelloul (1997), and because the interaction of the near-inertial disturbances with geostrophic flow is a crucial oceanic process (Kunze 1985; Klein *et al.* 2004).

3.1. *Scaling assumptions*

Now we reduce the linear problem in (3.8)–(3.12) using the assumption that (u, v, w, p, b) is a slowly modulated near-inertial disturbance. This requires three assumptions. First, the time dependence of both the geostrophic component, B_g, and the pump modulation, $\tilde{B}_p$, is slow relative to the inertial time scale f_0^{-1}. The second assumption is that the amplitude of the background flow is 'small'. Small means that the horizontal velocities of the background flows are much less than the phase speed of the first baroclinic mode, c_1, or equivalently that buoyancy perturbations B_p and B_g are much less than the resting stratification $N^2(z)$. The third assumption is that the vertical scale of B_g and B_p is comparable to the depth of the ocean H, e.g. the background-state fields have a vertical mode-one structure. There is no assumption concerning separation in horizontal scale between the background flow and the near-inertial disturbance.

To formalize the assumptions above, we non-dimensionalize the Boussinesq equations using H to denote the depth of the ocean and N_0 as a scale of the buoyancy frequency $N(z)$, e.g. N_0 might be the vertical average of $N(z)$. We introduce a small non-dimensional parameter ϵ defined by

$$B_{p,g} = \epsilon^2 \times N_0^2 H \times \text{non-dimensional}(B_{p,g}), \quad \text{(definition of } \epsilon\text{)}. \tag{3.13}$$

As an example, consider a progressive internal tidal wavetrain propagating northward in the Pacific Ocean with an energy flux of order $1\,\mathrm{kW\,m^{-1}}$. Rough estimates show that the horizontal velocities of the internal tidal wave, U_p, are between 10 and $20\,\mathrm{cm\,s^{-1}}$, while the phase speed of vertical mode one, c_1, is between 2 and $4\,\mathrm{m\,s^{-1}}$. In this case $\epsilon \equiv \sqrt{U_p/c_1}$ is between 0.16 and 0.32.

As a consequence of the assumptions above, the near-inertial fields evolve on a 'slow time scale' $(\epsilon^2 f_0)^{-1} \gg f_0^{-1}$. The geostrophic flow, and the envelope of the $2f_0$-pump, might also evolve on the slow time scale: a main assumption is the existence of a spectral gap between the inertial peak and the low-frequency evolution of background.

To non-dimensionalize x and y we introduce $L \equiv N_0 H / f_0$, which is proportional to the first deformation length. We assume that the base-state fields vary vertically on the scale H while the near-inertial fields vary vertically on a scale $h \ll H$, where

$$h \equiv \epsilon H. \tag{3.14}$$

https://doi.org/10.1017/S0022112008001742 Published online by Cambridge University Press

Thus, ϵ defined in (3.13) characterizes the separation in vertical scale between the background fields (U, V, W, B, P) and the near-inertial fields (u, v, w, b, p). This separation in vertical scale is evident in figure 1. The non-dimensional independent variables, with hats, are then defined by

$$(x, y) = L\,(\hat{x}, \hat{y}), \qquad z = h\hat{z}, \qquad \hat{t} = f_0 t. \tag{3.15}$$

Because the vertical coordinate has been scaled with h, the ocean depth is $O(\epsilon^{-1})$ in terms of $\hat{z}$. Other non-dimensional variables are

$$N(z) = N_0 \hat{N}(\epsilon\hat{z}), \qquad f = f_0(1 + \epsilon^2\hat{\beta}\hat{y}), \tag{3.16}$$

where $\hat{\beta} = L\beta/\epsilon^2 f_0$; this scaling ensures that the variation of f over the distance L is comparable to the low frequency $\epsilon^2 f_0$ which characterizes the other sub-inertial processes. The base-state fields have the form

$$(U, V) = \epsilon^2 f_0 L\,(\hat{U}, \hat{V}), \qquad W = \epsilon^2 f_0 H\,\hat{W}, \qquad B = \epsilon^2 N_0^2 H\,\hat{B}, \tag{3.17}$$

where the background flow $(\hat{U}, \hat{V}, \hat{W}, \hat{B})$, like $\hat{N}$, depends on the vertical coordinate only through

$$\hat{z}_1 \equiv \epsilon\hat{z}. \tag{3.18}$$

Thus, for instance,

$$U_z = \epsilon^2 f_0 L^2 h^{-1} \hat{U}_{\hat{z}} = \epsilon^3 f_0 L^2 h^{-1} \hat{U}_{\hat{z}_1}. \tag{3.19}$$

Consequently, in the final scaled equations, (3.21) below, the vertical derivatives of the background flow appear at higher orders than those of the near-inertial oscillations.

The near-inertial fields are non-dimensionalized as in Young & Ben Jelloul (1997):

$$(u, v) = f_0 L\,(\hat{u}, \hat{v}), \qquad w = f_0 h\,\hat{w}, \qquad b = N_0^2 h\,\hat{b}, \qquad p = \epsilon^2 f_0^2 L^2\,\hat{p}. \tag{3.20}$$

The most important point here is the ϵ^2 in the definition of $\hat{p}$: this ensures that the near-inertial pressure gradient does not appear at leading order.

3.2. *The scaled equations*

Suppressing the hats, the scaled version of (3.8)–(3.12) is

$$\left.\begin{aligned}
&u_t - v + \epsilon(Wu)_z + \epsilon^2[u_{t_2} + Uu_x + Vu_y + uU_x + vU_y - W_{z_1}u - \beta yv + p_x] \\
&\quad + \epsilon^3 wU_{z_1} = 0, \\
&v_t + u + \epsilon(Wv)_z + \epsilon^2[v_{t_2} + Uv_x + Vv_y + uV_x + vV_y - W_{z_1}v + \beta yu + p_y] \\
&\quad + \epsilon^3 wV_{z_1} = 0, \\
&p_z - b = 0, \\
&u_x + v_y + w_z = 0, \\
&b_t + wN^2 + \epsilon[uB_x + vB_y + (Wb)_z] + \epsilon^2[b_{t_2} + Ub_x + Vb_y + wB_{z_1} - W_{z_1}b] = 0.
\end{aligned}\right\} \tag{3.21}$$

In anticipation of secularity at second order, we have introduced the slow time $t_2 \equiv \epsilon^2 t$ corresponding to the time scale $(\epsilon^2 f_0)^{-1}$ mentioned previously. One other point requiring comment in (3.21) is that terms involving vertical advection by W have been split like this:

$$Wu_z = (Wu)_z - \epsilon W_{z_1} u. \tag{3.22}$$

Because of the small vertical scale of the near-inertial flow, the terms $(Wu)_z$ and $(Wv)_z$ occur early in the expansion and the total vertical derivative eases some technical difficulties adumbrated in the discussion surrounding (3.41).

https://doi.org/10.1017/S0022112008001742 Published online by Cambridge University Press

The algebra is simplified if we use the complex combinations

$$\mathscr{U} \equiv u + \mathrm{i}v, \quad \xi \equiv x + \mathrm{i}y. \tag{3.23}$$

Horizontal derivatives can be expressed in terms of ξ and ξ^* using

$$\partial_\xi = \tfrac{1}{2}(\partial_x - \mathrm{i}\partial_y), \quad \partial_{\xi^*} = \tfrac{1}{2}(\partial_x + \mathrm{i}\partial_y)\,; \tag{3.24}$$

the horizontal Laplacian is $\partial_x^2 + \partial_y^2 = 4\partial_\xi \partial_{\xi^*}$. The divergence and vertical vorticity are conveniently obtained from $\mathscr{U}_\xi = (u_x + v_y)/2 + \mathrm{i}(v_x - u_y)/2$. We proceed by solving (3.21) with a perturbation expansion

$$\mathscr{U} = \mathscr{U}_0 + \epsilon \mathscr{U}_1 + \epsilon^2 \mathscr{U}_2 + O(\epsilon^3). \tag{3.25}$$

3.3. *Leading order:* ϵ^0

The leading-order system

$$\partial_t \mathscr{U}_0 + \mathrm{i}\mathscr{U}_0 = 0, \tag{3.26}$$
$$p_{0z} - b_0 = 0, \tag{3.27}$$
$$u_{0x} + v_{0y} + w_{0z} = 0, \tag{3.28}$$
$$\partial_t b_0 + w_0 N^2 = 0, \tag{3.29}$$

is solved with

$$\mathscr{U}_0 = L A\, \mathrm{e}^{-\mathrm{i}f_0 t}, \tag{3.30}$$
$$w_0 = -f_0^2 N^{-2} A_{\xi z}\, \mathrm{e}^{-\mathrm{i}f_0 t} + \text{c.c.}, \tag{3.31}$$
$$b_0 = \mathrm{i} f_0 A_{z\xi} \mathrm{e}^{-\mathrm{i}f_0 t} + \text{c.c.}, \tag{3.32}$$
$$p_0 = \mathrm{i} f_0 A_\xi \mathrm{e}^{-\mathrm{i}f_0 t} + \text{c.c.} \tag{3.33}$$

Above, $A(\boldsymbol{x}, t_2)$ is a complex amplitude and $L \equiv \partial_z f_0^2 N^{-2} \partial_z$ is a differential operator. For reference in (3.30)–(3.33) we have reverted to dimensional variables; the non-dimensional leading order is obtained with $f_0 \to 1$. The boundary condition that w_0 vanish at the top and bottom is satisfied by requiring that $A_z = 0$ at these boundaries.

3.4. *First order:* ϵ^1

At order ϵ the equations are:

$$\partial_t \mathscr{U}_1 + \mathrm{i}\mathscr{U}_1 = -(W\mathscr{U}_0)_z, \tag{3.34}$$
$$p_{1z} - b_1 = 0, \tag{3.35}$$
$$u_{1x} + v_{1y} + w_{1z} = 0, \tag{3.36}$$
$$\partial_t b_1 + w_1 N^2 = -u_0 B_x - v_0 B_y - (W b_0)_z. \tag{3.37}$$

There are no resonant terms in (3.34). Explicitly, using W in (3.7), and the leading-order expression for $\mathscr{U}_0$ in (3.30), we have from (3.34):

$$\mathscr{U}_1 = \tfrac{1}{2}\mathrm{i}[(\tilde{W}_p^* \mathrm{e}^{\mathrm{i}t} - \tilde{W}_p \mathrm{e}^{-3\mathrm{i}t}) L A]_z. \tag{3.38}$$

The better part of valour is to calculate w_1 by integrating the continuity equation

$$w_{1z} = -\mathscr{U}_{1\xi} - \mathscr{U}_{1\xi^*}^* \tag{3.39}$$

with respect to z. In this vertical integration there is only one constant of integration and two boundary conditions: w_1 must be zero at both $z = 0$ and $z = -H$. Thus

https://doi.org/10.1017/S0022112008001742 Published online by Cambridge University Press

integrating (3.39) between $z=-H$ and $z=0$ gives:

$$\int_{-H}^{0} \mathscr{U}_{1\xi} + \mathscr{U}^{*}_{1\xi^{*}}\,\mathrm{d}z = 0\,; \tag{3.40}$$

this solvability condition is guaranteed if

$$\int_{-H}^{0} \mathscr{U}_1\,\mathrm{d}z = 0. \tag{3.41}$$

Because $\mathscr{U}_1$ in (3.38) is a total vertical derivative, and $\tilde{W}_p$ is zero at the boundaries, the solvability condition (3.41) is satisfied by $\mathscr{U}_1$ in (3.38). Thus, we possess a consistent expression for w_1 in terms of A.

3.5. *Second order:* ϵ^2

At second order, ϵ^2, the momentum equations are:

$$\begin{aligned}\partial_t \mathscr{U}_2 + \mathrm{i}\mathscr{U}_2 + (W\mathscr{U}_1)_z + \partial_{t_2}\mathscr{U}_0 + U\mathscr{U}_{0x} + V\mathscr{U}_{0y} \\ + (U_x + \mathrm{i}V_x)u_0 + (U_y + \mathrm{i}V_y)v_0 - W_{z_1}\mathscr{U}_0 + \mathrm{i}\beta y\mathscr{U}_0 + 2p_{0\xi^{*}} = 0.\end{aligned} \tag{3.42}$$

Terms proportional to $\exp(-\mathrm{i}t)$ in (3.42) drive $\mathscr{U}_2$ resonantly. For instance,

$$\begin{aligned}(U_x + \mathrm{i}V_x)u_0 + (U_y + \mathrm{i}V_y)v_0 &= \tfrac{1}{2}\mathscr{U}_0[U_x + V_y + \mathrm{i}V_x - \mathrm{i}U_y] + \tfrac{1}{2}\mathscr{U}^{*}_0[U_x - V_y + \mathrm{i}V_x + \mathrm{i}U_y], \\ &= LA^{*}(\tilde{U}_p + \mathrm{i}\tilde{V}_p)_{\xi^{*}}\mathrm{e}^{-\mathrm{i}t} + \mathrm{NRT},\end{aligned} \tag{3.43}$$

and

$$\begin{aligned}W\mathscr{U}_1 &= (\tilde{W}^{*}_p\mathrm{e}^{2\mathrm{i}t} + \tilde{W}_p\mathrm{e}^{-2\mathrm{i}t})\frac{\mathrm{i}}{2}[(\tilde{W}^{*}_p\,\mathrm{e}^{\mathrm{i}t} - \tilde{W}_p\,\mathrm{e}^{-3\mathrm{i}t})LA]_z, \\ &= \frac{\mathrm{i}}{2}\big(\tilde{W}_p\tilde{W}_{pz}{}^{*} - \tilde{W}_p{}^{*}\tilde{W}_{pz}\big)LA\,\mathrm{e}^{-\mathrm{i}t} + \mathrm{NRT},\end{aligned} \tag{3.44}$$

where NRT stands for non-resonant terms.

3.6. *The evolution equation for the near-inertial fields*

Elimination of the $\mathrm{e}^{-\mathrm{i}t}$-resonant terms in (3.42), and restoration of dimensions, produces the evolution equation

$$LA_t + (\varpi LA)_z + J(\psi, LA) + \mathrm{i}\left(\beta y + \tfrac{1}{2}\zeta\right)LA + \tfrac{1}{2}\mathrm{i}f_0\nabla^2 A + \tfrac{1}{2}\Upsilon LA^{*} = 0, \tag{3.45}$$

where $\nabla^2 = \partial_x^2 + \partial_y^2$ is the horizontal Laplacian and $J(a,b) = a_x b_y - a_y b_x$ is a Jacobian. The streamfunction ψ in (3.45) is defined in (3.5) and $\zeta \equiv \nabla^2\psi$ is the relative vorticity. These terms involving the geostrophic part of the background flow are familiar from Young & Ben Jelloul (1997) and Klein *et al.* (2004). The new terms in (3.45) arising from the $2f_0$-pump are those involving

$$\varpi \equiv \frac{\mathrm{i}}{2f_0}\big(\tilde{W}_p\tilde{W}_{pz}{}^{*} - \tilde{W}^{*}_p\tilde{W}_{pz}\big), \tag{3.46}$$

and

$$\Upsilon \equiv 2(\tilde{U}_p + \mathrm{i}\tilde{V}_p)_{\xi^{*}} = \tilde{U}_{px} - \tilde{V}_{py} + \mathrm{i}\big(\tilde{V}_{px} + \tilde{U}_{py}\big). \tag{3.47}$$

The vertical velocity ϖ in (3.45) and (3.46) results from rectified vertical heaving; numerical estimates in §§ 4 and 5 indicate that ϖ is small, or zero, so that $(\varpi LA)_z$ does not have a palpable effect on the evolution of A. In fact, $(\varpi LA)_z$ scales like $\epsilon^3 f_0 LA$ while the other terms in (3.45) scale like $\epsilon^2 f_0 LA$. The rectified vertical advection,

https://doi.org/10.1017/S0022112008001742 Published online by Cambridge University Press

$(\varpi LA)_z$, has been promoted to higher order by our decision to represent vertical derivatives as in (3.22). This has the advantage of producing first-order fields which satisfy the solvability condition in (3.41), but it does lead to some mixing of orders in (3.45).

The essential new physics in (3.45) is introduced by $\Upsilon LA^*/2$. The expression for the pump strength Υ in (3.47) is identical to the earlier, heuristic result for Υ in (2.7). Thus, the new term is a near-inertial energy source produced by PSI.

4. Near-inertial PSI of a plane internal wave

4.1. *The pump wave*

As an application of (3.45) we consider the most basic example of inertially resonant PSI: the instability of a plane wave with uniform stratification on an f-plane (i.e. $\beta = 0$). Thus, as a specific model of the pump, we consider an infinite-plane internal gravity wave with pressure

$$P_p = a\cos\phi, \tag{4.1}$$

where $\phi \equiv kx + mz - \omega t$ and the parameter a, with dimensions (length/time)^2, controls the amplitude of the pump. The frequency and wavenumber are related by the hydrostatic dispersion relation

$$\omega^2 = f_0^2 + N^2\frac{k^2}{m^2}. \tag{4.2}$$

Since ω is close to $2f_0$ we write

$$\omega = 2f_0 + \sigma, \qquad \sigma \ll f_0, \tag{4.3}$$

where the de-tuning frequency, σ, might be either positive or negative. In § 4.3, the special case of a resonant triad is recovered by taking $\sigma = 0$.

Substituting the pressure into the Boussinesq equations, we obtain the other pump fields:

$$U_p = \frac{ak\omega}{\omega^2 - f_0^2}\cos\phi, \qquad V_p = \frac{akf_0}{\omega^2 - f_0^2}\sin\phi, \tag{4.4}$$

and

$$W_p = -\frac{ak^2\omega}{m(\omega^2 - f_0^2)}\cos\phi, \qquad B_p = -am\sin\phi. \tag{4.5}$$

Thus

$$U_{px} + \mathrm{i}V_{px} = \frac{\mathrm{i}ak^2\mathrm{e}^{\mathrm{i}\phi}}{2(\omega - f_0)} - \frac{\mathrm{i}ak^2\mathrm{e}^{-\mathrm{i}\phi}}{2(\omega + f_0)}, \tag{4.6}$$

and therefore

$$\Upsilon = \overline{\mathrm{e}^{2\mathrm{i}f_0 t}(U_{px} + \mathrm{i}V_{px})} = \mathrm{i}\upsilon\mathrm{e}^{\mathrm{i}(kx+mz-\sigma t)}, \tag{4.7}$$

where

$$\upsilon \equiv \frac{ak^2}{2(\omega - f_0)} \approx \frac{ak^2}{2f_0}. \tag{4.8}$$

The other parameter in the amplitude equation (3.45) is ϖ defined in (3.46). With W_p in (4.5) we obtain

$$\varpi = \frac{1}{4mf_0}\left(\frac{ak^2\omega}{\omega^2 - f_0^2}\right)^2 \approx \frac{1}{9}\frac{a^2k^4}{mf_0^3}. \tag{4.9}$$

https://doi.org/10.1017/S0022112008001742 Published online by Cambridge University Press

Order of magnitude estimates using numerical values, such as those in (4.20)–(4.22), indicate that ϖ is less than $10^{-5}\,\mathrm{m\,s^{-1}}$. This is too small to affect the solution significantly; thus we now neglect the term $(\varpi LA)_z$.

4.2. *Solution of the evolution equation*

With uniform N, $\beta = 0$, and using Υ in (4.7), the evolution equation (3.45) is

$$A_{zzt} + \frac{\mathrm{i}N^2}{2f_0}A_{xx} + \frac{\mathrm{i}\upsilon}{2}\mathrm{e}^{\mathrm{i}(kx+mz-\sigma t)}A^*_{zz} = 0. \tag{4.10}$$

Equation (4.10) has solutions of the form

$$A = \mathrm{e}^{-\mathrm{i}\sigma t/2}\left[A_1(t)\mathrm{e}^{\mathrm{i}(k_1x+m_1z)} + A^*_2(t)\mathrm{e}^{\mathrm{i}(k_2x+m_2z)}\right], \tag{4.11}$$

provided that

$$k_1 + k_2 = k, \qquad m_1 + m_2 = m. \tag{4.12}$$

Substituting (4.11) into (4.10) gives

$$A_{1t} + \mathrm{i}\omega_1 A_1 + \frac{\mathrm{i}\upsilon m_2^2}{2m_1^2}A_2 = 0, \tag{4.13}$$

$$A_{2t} - \mathrm{i}\omega_2 A_2 - \frac{\mathrm{i}\upsilon m_1^2}{2m_2^2}A_1 = 0, \tag{4.14}$$

where

$$\omega_n \equiv \frac{N^2}{2f_0}\frac{k_n^2}{m_n^2} - \frac{\sigma}{2} \qquad \text{with} \qquad n = 1, 2. \tag{4.15}$$

We obtain a single equation for $A_1(t)$:

$$A_{1tt} + \mathrm{i}(\omega_1 - \omega_2)A_{1t} + \left(\omega_1\omega_2 - \frac{\upsilon^2}{4}\right)A_1 = 0, \tag{4.16}$$

and if $A_1 = \hat{A}_1 \exp(st)$ then

$$s = \tfrac{1}{2}(\omega_2 - \omega_1)\mathrm{i} \pm \tfrac{1}{2}\sqrt{\upsilon^2 - (\omega_1 + \omega_2)^2}. \tag{4.17}$$

The growth rate is $\gamma = \mathrm{Re}(s)$, or

$$\gamma = \tfrac{1}{2}\sqrt{\upsilon^2 - \left(\frac{N^2}{2f_0}\right)^2\left(\frac{k_1^2}{m_1^2} + \frac{k_2^2}{m_2^2} - 2\frac{\sigma f_0}{N^2}\right)^2}. \tag{4.18}$$

We now discuss the consequences of (4.18).

4.3. *Perfect resonance: $\omega = 2f_0$*

If the resonance is perfectly tuned, i.e. if $\sigma = 0$ in (4.3), then the solution in (4.11) and (4.12) is a resonant triad and γ in (4.18) achieves the maximum value,

$$\gamma_{max} \equiv \frac{\upsilon}{2} = \frac{ak^2}{4f_0}, \tag{4.19}$$

by letting $m_1 \to \pm\infty$ and $m_2 \to \mp\infty$ with the sum $m_1 + m_2$ fixed at m. In this limit the values of k_1 and k_2 in (4.18) are irrelevant because $(k_n/m_n)^2 \to 0$. Figure 2 shows the growth rate (4.18) contoured in the (k_1, m_1)-plane. Because there is no high wavenumber cutoff, the prediction is that a broad band of near-inertial high-vertical-wavenumber oscillations are excited by PSI: with perfect resonance the instability does not select a particular vertical scale.

https://doi.org/10.1017/S0022112008001742 Published online by Cambridge University Press

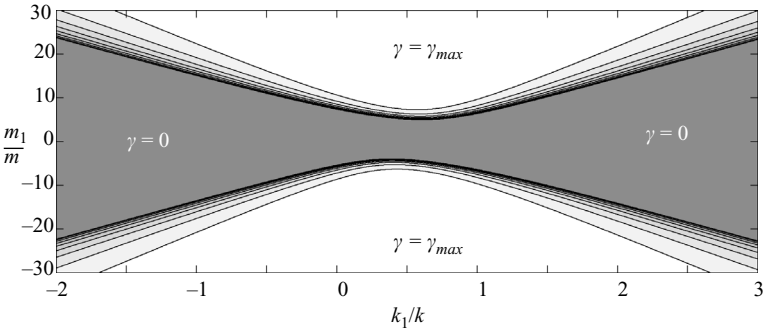


FIGURE 2. Growth rate γ obtained from (4.18) as a function of m_1/m and k_1/k, where (k, m) is the wavenumber of the pump wave. In this illustration the resonance is perfectly tuned, i.e. $\sigma = 0$. The other parameter values are $N = 28\,f_0$, $k = 2\pi/(129\,\mathrm{km})$, $m = \pi/(4\,\mathrm{km})$ and $a = 0.1551\,\mathrm{m^2\,s^{-2}}$. Short waves with large values of m_1/m grow at the rate γ_{max} in (4.19).

Order of magnitude estimates show that the instability is fast. For example, to match roughly the parameters used by MacKinnon & Winters (2007) in their simulation of a North Pacific internal tide, we take

$$\omega = M_2 = 1.41 \times 10^{-4}\,\mathrm{s^{-1}}, \qquad f_0 = \tfrac{1}{2}M_2, \qquad N = 28\,f_0, \qquad m = \frac{\pi}{4000\,\mathrm{m}}. \tag{4.20}$$

Using the internal wave dispersion relation, the horizontal wavelength of the pump wave is $2\pi/k = 129\,\mathrm{km}$. To set the amplitude of the pump wave we take

$$a = 0.1551\,\mathrm{m^2 s^{-2}}, \tag{4.21}$$

in (4.1). Then the root mean square pump velocities are

$$\sqrt{\overline{U_p^2}} = 5.05\,\mathrm{cm\,s^{-1}}, \qquad \sqrt{\overline{V_p^2}} = 2.53\,\mathrm{cm\,s^{-1}}, \tag{4.22}$$

and the root-mean-square vertical excursion of the isopycnals is 22.4 m.

From (4.19), it follows that

$$\frac{1}{\gamma_{max}} = 8.9\,\mathrm{days}. \tag{4.23}$$

This 8.9 day *e*-folding agrees in order of magnitude with the numerical results of Hibiya *et al.* (2002) and MacKinnon & Winters (2005). MacKinnon & Winters argue heuristically that the growth rate of PSI is

$$\gamma \sim k\sqrt{\overline{U_p^2}}. \tag{4.24}$$

Our expression for γ_{max} in (4.19) is equivalent to

$$\gamma_{max} = \frac{3k}{4\sqrt{2}}\sqrt{\overline{U_p^2}} = \frac{3k}{2\sqrt{10}}\sqrt{\overline{U_p^2} + \overline{V_p^2}}; \tag{4.25}$$

thus the scaling argument of MacKinnon & Winters is vindicated and made precise by the numerical factors on the right-hand side of (4.25).

Olbers & Pomphrey (1981) examined the wave–wave interaction between the M_2 internal tide and the internal wave continuum and estimated the time scale for energy transfer from low vertical modes via PSI to be $O(100)$ days. Presumably the

https://doi.org/10.1017/S0022112008001742 Published online by Cambridge University Press

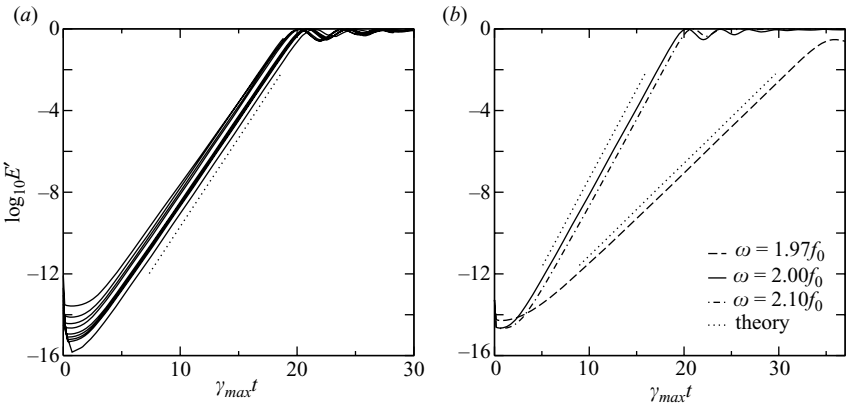


FIGURE 3. (*a*) Exponential growth of the normalized disturbance energy, E' defined in (A 8). The figure shows nine runs, all with $\sigma = 0$, and different values of a between $0.0388\,\mathrm{m^2\,s^{-2}}$ and $0.6203\,\mathrm{m^2\,s^{-2}}$. The numerical results are condensed by using $\gamma_{max}t$ as the abscissa; the dashed line indicates the theoretical prediction $\exp(2\gamma_{max}t)$, with γ_{max} given by (4.19). (*b*) Exponential growth of normalized perturbation energy E' with slight de-tuning. If $\sigma > 0$, as in the case $\omega = 2.1f_0$ above, then the perturbation grows at the rate $\gamma_{max} = \upsilon/2$. In the case with $\sigma < 0$ (for example $\omega = 1.97f_0$ above) then the growth rate is reduced to $\sqrt{\upsilon^2 - \sigma^2}/2$.

order-of-magnitude difference between this estimate and the numbers above results from the random-phase assumption made by Olbers & Pomphrey.

A main prediction is that with perfect resonance there is no vertical scale selection: the fastest-growing near-inertial disturbances have infinite vertical wavenumber and grow at the rate γ_{max}. This indicates that PSI is a potent mechanism for transferring energy directly to small vertical scales, which is good for mixing. On the other hand, lack of vertical scale selection is disquieting. Thus it is reassuring to test these predictions by comparing them with the results of a numerical solution of the full nonlinear Boussinesq equations. To do this efficiently we solve the Boussinesq equations in the (x, z)-plane using the streamfunction–vorticity formulation summarized in Appendix A. The initial condition is the plane wave in (4.1), plus very small random noise which is subsequently amplified by PSI. Figure 3(*a*) shows that in the resonant case the growth of the near-inertial disturbances is correctly predicted by (4.19).

4.4. *PSI with* $\omega > 2f_0$

If the pump frequency slightly exceeds $2f_0$ then the resonance is de-tuned, and the strength of the de-tuning, σ/f_0, changes the growth rate of PSI. Figure 4 shows the growth rate (4.18) contoured in the (k_1, m_1)-plane. Figure 5 shows the growth rate as a function of m_1/m along the line $k_1/k = 2$. If the de-tuning is large enough (e.g. $\sigma/f_0 = 0.05$ in figures 4*b* and 5*a*) then there is a high-m_1 cutoff.

Despite the structural changes in $\gamma(k_1, m_1)$ induced by σ, a main point is that if σ is positive, then there are always waves which achieve the growth rate γ_{max} in (4.19). For example, in the numerical solution shown in figure 3(*b*), the disturbance energy in the de-tuned case with $\omega/f_0 = 2.1$, grows at the same rate as the disturbance in the resonant case, $\omega/f_0 = 2$: both disturbances amplify as $\exp(\gamma_{max}t)$.

The derivation of the amplitude equation assumes vertical scale separation between the pump wave and the near-inertial response, i.e. that $m_1/m \gg 1$. However,

https://doi.org/10.1017/S0022112008001742 Published online by Cambridge University Press

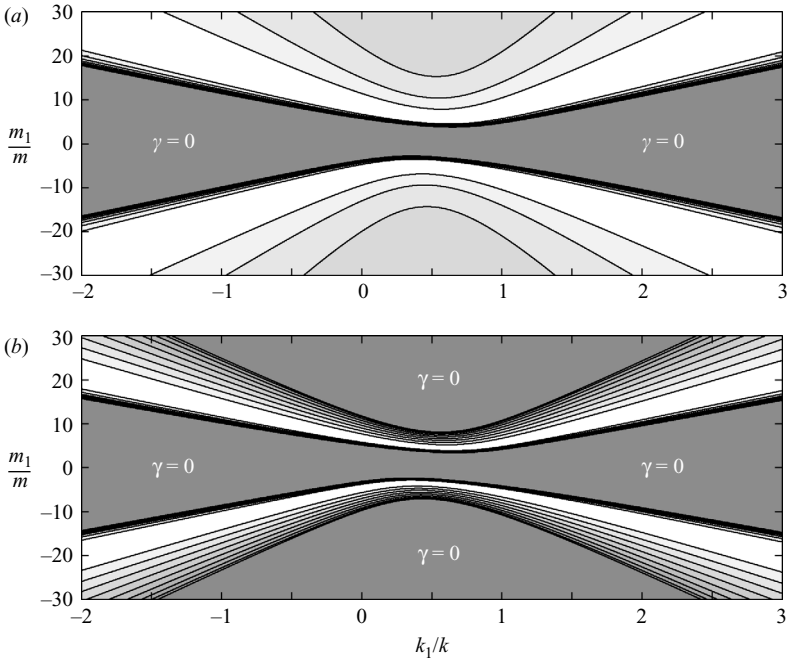


FIGURE 4. Growth rate γ obtained from (4.18) as a function of m_1/m and k_1/k, where (k, m) is the wavenumber of the pump wave. (*a*) ($\sigma/f_0 = 0.003$) The growth rate asymptotes to $\sqrt{\upsilon^2 - \sigma^2}/2$ as $m_1/m \to \infty$ with k_1/k fixed; see the curve labelled $\sigma/f_0 = 0.03$ in figure 5(*a*). (*b*) ($\sigma/f_0 = 0.05$) With larger de-tuning so that $\sigma^2 > \upsilon^2$, the instability is cut off as $m_1/m \to \infty$ with k_1/k fixed; see the curve labelled $\sigma/f_0 = 0.05$ in figure 5(*a*).

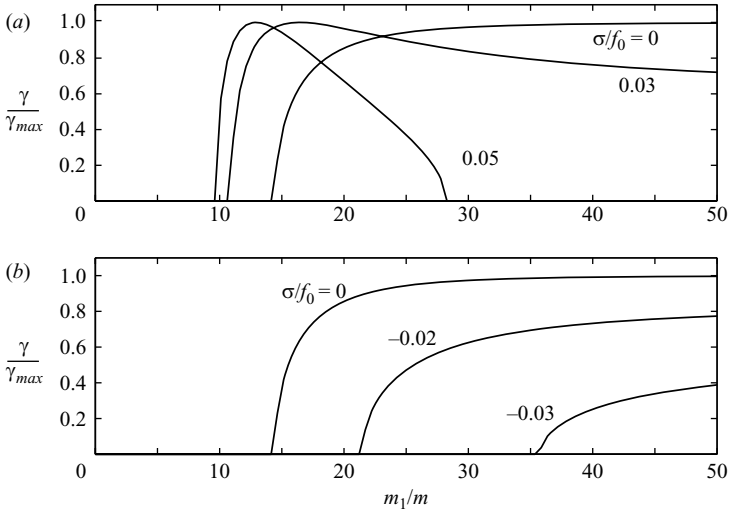


FIGURE 5. Growth rate from (4.18) as a function of m_1/m with $k_1/k = 2$. Panel (*a*): the case $\sigma/f_0 \geqslant 0$; the three curves all have maximum growth rate given by γ_{max} in (4.19). Panel (*b*) the case $\sigma/f_0 \leqslant 0$. Note that as σ becomes more negative, unstable disturbances move to higher wavenumbers and the growth rate is reduced. The instability disappears if $-\sigma > \upsilon$.

figure 5(*a*) shows that the instability moves to smaller values of m_1/m as the de-tuning is increased. Thus the quantitative validity of (4.18) for largish values of σ/f_0 is uncertain.

https://doi.org/10.1017/S0022112008001742 Published online by Cambridge University Press

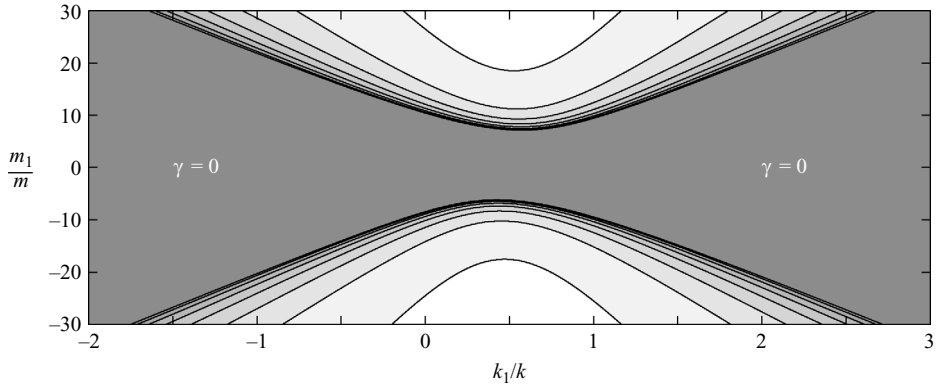


FIGURE 6. Growth rate γ obtained from (4.18) as a function of m_1/m and k_1/k, where (k, m) is the wavenumber of the pump wave. In this illustration $\sigma/f_0 = -0.02$ and γ asymptotes to $\frac{1}{2}\sqrt{\upsilon^2 - \sigma^2} < \gamma_{max}$ at large wavenumbers.

4.5. *PSI with $\omega < 2f_0$*

Finally, suppose that the pump frequency, ω, is less than $2f_0$ so that σ/f_0 is negative. In this case, the subharmonic, $\omega/2$, falls outside the usual band of internal wave frequencies and according to resonant interaction theory there should be no PSI. Nonetheless, (4.18) indicates that subinertial, unstable disturbances exist. Thus, (3.45) predicts that PSI extends the internal wave band to slightly subinertial frequencies. Figures 6 and 5(*b*) indicate that the growth rate is reduced relative to the case with $\sigma > 0$, and the instability is shifted to higher wavenumbers. Again there is no vertical scale selection: as $m/m_1 \to \infty$, the growth rate γ asymptotes to $\frac{1}{2}\sqrt{\upsilon^2 - \sigma^2} < \gamma_{max}$. Numerical simulation confirms the existence of slightly subinertial disturbances that amplify with a reduced growth rate, e.g. see the curve $\omega = 1.97 f_0$ in figure 3(*b*).

5. Near-inertial PSI of a mode-one wavetrain

In §4, we considered the parametric instability of a plane wave with uniform buoyancy frequency. The main advantage of this model is that the linear stability problem can be solved exactly and simple expressions for the growth rate are obtained, e.g. as in (4.18) and (4.25). In this section, we take a step in the direction of greater realism by analysing the parametric instability of a train of internal gravity waves with mode-one structure in the vertical. We use a non-uniform buoyancy frequency, $N(z)$, proposed by Gill (1984) and summarized in Appendix B. A key feature of Gill's model stratification is realistic surface intensification below a mixed layer. The modal phase speeds, and sample eigenfunctions, are shown in figure 7.

5.1. *The pump wavetrain*

As §4, the frequency of the primary pump wave is ω, the horizontal wavenumber is k and the pressure is ρ_0 times

$$P_p = a\,\cos(kx - \omega t)\,p_1(z). \tag{5.1}$$

Above, $p_1(z)$ is the vertical mode-one eigenfunction, and a is the amplitude (with units of $\mathrm{m^2\,s^{-2}}$). For the details of $p_1(z)$ see Appendix B. Again we assume that ω is close to twice the local inertial frequency and we define a de-tuning frequency σ by (4.3), i.e. $\sigma = \omega - 2f_0$. The horizontal velocities associated with the pressure field in

https://doi.org/10.1017/S0022112008001742 Published online by Cambridge University Press

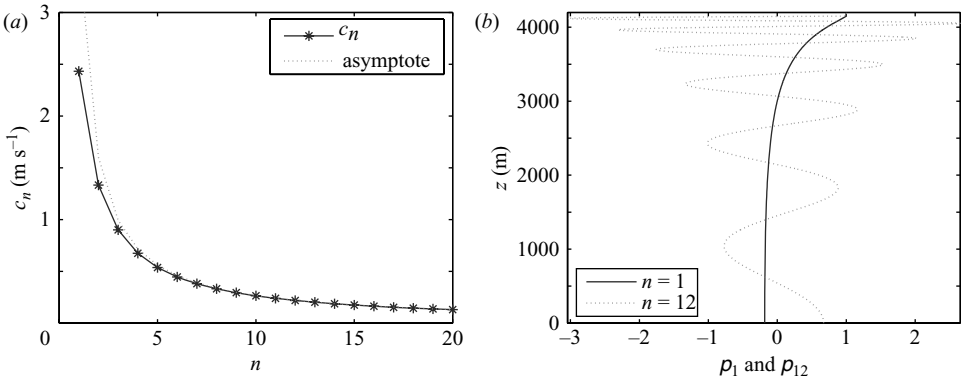


FIGURE 7. (*a*) Modal phase speeds, c_n, obtained from (B 7) and (B 8) using the numerical values in table 1. The dotted curve is the large-n approximation $c_n \approx 2s/\sqrt{1+(2n+1)^2\pi^2/\xi_T^2}$. (*b*) The eigenmodes $p_1(z)$ and $p_{12}(z)$; note surface intensification.

(5.1) are

$$U_p = \frac{ka\omega}{\omega^2 - f_0^2}\cos(kx-\omega t)p_1(z), \qquad V_p = \frac{kaf_0}{\omega^2 - f_0^2}\sin(kx-\omega t)p_1(z). \tag{5.2}$$

The pump amplitude is obtained by substituting (5.2) into (3.47):

$$\Upsilon(x,z,t) = \mathrm{i}\upsilon \mathrm{e}^{\mathrm{i}(kx-\sigma t)}\, p_1(z), \tag{5.3}$$

where $\upsilon = ak^2/2f_0$. For a pump wave whose vertical structure is a single vertical mode as in (5.1), ϖ in (3.45) is identically zero.

5.2. *Solution method*

Taking $\psi = \zeta = \beta = 0$, we solve the amplitude equation in (3.45) using a modal decomposition,

$$A = e^{-\mathrm{i}\sigma t/2}\left[A_1(z,t)e^{\mathrm{i}k_1 x} + A_2^*(z,t)e^{\mathrm{i}k_2 x}\right], \tag{5.4}$$

where $k_1 + k_2 = k$. This yields the coupled equations,

$$\begin{aligned} L\left(A_{1t} - \tfrac{1}{2}\mathrm{i}\sigma A_1\right) - \tfrac{1}{2}\mathrm{i}f_0 k_1^2 A_1 + \tfrac{1}{2}\mathrm{i}\upsilon p_1(z) L A_2 = 0,\\ L\left(A_{2t} + \tfrac{1}{2}\mathrm{i}\sigma A_2\right) + \tfrac{1}{2}\mathrm{i}f_0 k_2^2 A_2 - \tfrac{1}{2}\mathrm{i}\upsilon p_1(z) L A_1 = 0, \end{aligned} \tag{5.5}$$

which must be solved subject to the boundary conditions, $A_{1z}(0,t) = A_{1z}(H,t) = A_{2z}(0,t) = A_{2z}(H,t) = 0$. We represent the variables $A_1(z,t)$ and $A_2(z,t)$, as modal sums:

$$A_j(z,t) = e^{st}\sum_{n=1}^{\infty} c_n^2 a_{jn} p_n(z). \tag{5.6}$$

The L-operation then simply multiplies each of the relevant terms in the sum by the factor, $-f_0^2/c_n^2$, where c_n is the modal phase speed defined in (B 2). We now multiply each of (5.5) by $p_n(z)$ and integrate in z, using the orthogonality relation (B 9)

$$\begin{aligned} s a_{1n} &= -\tfrac{1}{2}\mathrm{i}\left(f_0^{-1}k_1^2 c_n^2 - \sigma\right)a_{1n} - \tfrac{1}{2}\mathrm{i}\upsilon\sum_{n'=1}^{\infty} M_{nn'}a_{2n'},\\ s a_{2n} &= \tfrac{1}{2}\mathrm{i}\left(f_0^{-1}k_2^2 c_n^2 - \sigma\right)a_{2n} + \tfrac{1}{2}\mathrm{i}\upsilon\sum_{n'=1}^{\infty} M_{nn'}a_{1n'}, \end{aligned} \tag{5.7}$$

https://doi.org/10.1017/S0022112008001742 Published online by Cambridge University Press

where

$$M_{nn'} \equiv \int_0^H p_1 p_n p_{n'}\ \mathrm{d}z \Big/ \int_0^H p_n^2\ \mathrm{d}z. \tag{5.8}$$

Note that the barotropic mode, $n=0$, decouples from the problem at this stage and can be ignored. Hence, n and the sum over n' begin with the first baroclinic mode.

To proceed, we truncate the sums in (5.6) at $n=\mathscr{N}$ so that the matrix $M_{nn'}$ is $\mathscr{N}\times\mathscr{N}$; we also define two ($j=1$ and 2) diagonal, $\mathscr{N}\times\mathscr{N}$ matrices $\Omega^{(j)}_{nn'}$ by

$$\Omega^{(j)}_{nn'} \equiv \omega^{(j)}_n \delta_{nn'}, \tag{5.9}$$

where

$$\omega^{(j)}_n \equiv \frac{k_j^2 c_n^2}{2f_0} - \tfrac{1}{2}\sigma. \tag{5.10}$$

Thus, (5.7) turns into a $2\mathscr{N}\times 2\mathscr{N}$ matrix eigenvalue problem,

$$s\begin{pmatrix}\boldsymbol{a}_1\\ \boldsymbol{a}_2\end{pmatrix} = \mathrm{i}\begin{pmatrix}-\Omega^{(1)} & -\frac{1}{2}\upsilon M\\ \frac{1}{2}\upsilon M & \Omega^{(2)}\end{pmatrix}\begin{pmatrix}\boldsymbol{a}_1\\ \boldsymbol{a}_2\end{pmatrix}. \tag{5.11}$$

The matrix on the right-hand side of (5.11) is imaginary, and so the eigenvalues, s, are either purely imaginary or occur as complex pairs with frequency, ν, and growth rate, $\pm\gamma$, i.e. $s=\pm\gamma+\mathrm{i}\nu$.

5.3. *Results*

Eigenvalues, $s=\gamma-\mathrm{i}\nu$, obtained from (5.11) are shown in figure 8 for $\sigma=0$ and 2υ; the parameters used to obtain these solutions are given in table 1. Truncations of $\mathscr{N}=50$, 100, 200 and 400 in (5.11) are included in figure 8. The eigenfunctions of the most unstable modes with $\mathscr{N}=400$ are shown in figure 9.

Figure 8(*a*) shows the case with perfect resonance, i.e. $\sigma=0$. The solution develops increasingly small length scales as the truncation $\mathscr{N}$ is increased and consequently not all of the eigenvalues converge. In figure 8(*b*), with de-tuning $\sigma=2\upsilon$, convergence is rapid. This result can be rationalized by the form of the most unstable eigenfunction in figure 9: with $\sigma=0$, the vertical scale of the eigenfunction is very fine and becomes even finer if the resolution is increased. Thus, the eigenvalues are significantly influenced by the highest vertical modes included in the truncation (5.11). On the other hand, the eigenfunction for $\sigma=2\upsilon$ is dominated by vertical modes with $n\approx 10$ and convergence with increasing $\mathscr{N}$ is rapid. In both cases, the eigenfunction is concentrated in the upper ocean where the pump wave (5.1) has the largest amplitude.

The ultraviolet catastrophe at $\sigma=0$ is, once more, an indication of missing physics such as scale-selective dissipation, non-zero β or nonlinearity. We will not discuss these possibilities further. Instead, we emphasize that certain important aspects of the $\sigma=0$ case do approach definite limits as $\mathscr{N}$ increases. For example, figure 8 indicates that if $\sigma=0$, then the maximum growth rate converges to (4.19), i.e.

$$\gamma_{max} = \tfrac{1}{2}\upsilon = \frac{ak^2}{4f_0}. \tag{5.12}$$

This feature of the stability problem is illustrated further in figure 10, which displays the largest growth rate as a function of de-tuning, σ, again for various truncations. For $\sigma>\upsilon$, the eigenvalues are independent of $\mathscr{N}$, indicating that the largest growth

https://doi.org/10.1017/S0022112008001742 Published online by Cambridge University Press

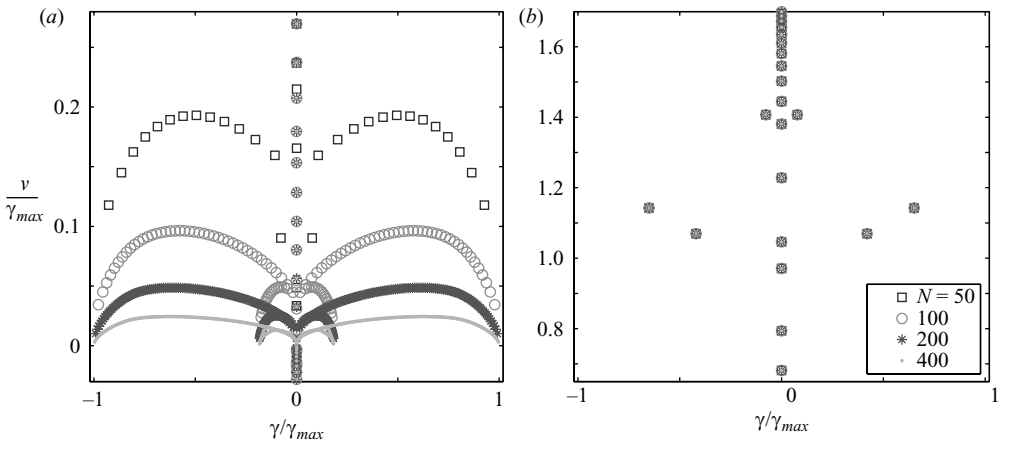


FIGURE 8. Eigenvalues, $s = \gamma - \mathrm{i}\nu$, plotted in the (γ, ν)-plane for four truncations $\mathscr{N}$ of (5.11) as indicated. In both panels $k_1 = 2k$, $k_2 = -k$ and $l_1 = l_2 = 0$. The results have been normalized by $\gamma_{max} \equiv \upsilon/2$. (*a*) Perfect resonance, $\sigma = 0$. The spectrum depends on the truncation. Despite this problem the growth rate of the most unstable mode converges slowly to γ_{max}. (*b*) Slight de-tuning, $\sigma = 2\upsilon$. Convergence is rapid as $\mathscr{N}$ increases.

Ocean depth, H	4200 m
Mixed layer depth, H_{mix}	50 m
Stratification parameter, z_0	4329.6 m
Stratification parameter, s	2.5 m s^{-1}
N at the base of mixed layer, $s/(z_0 - H + H_{mix})$	8 cycles per hour
Speed of first baroclinic mode, c_1	2.43 m s^{-1}
First deformation length, c_1/f_0	34.5 km
Normalization of mode one, $\int_0^H \rho_1^2(z)\,\mathrm{d}z$	329 m
Coriolis frequency, $f_0 = \frac{1}{2}M_2$	7.05×10^{-5} s^{-1}
Amplitude of the pump wave, a	0.1 m^2 s^{-2}
Wavenumber of the pump wave, $k = \sqrt{3}f_0/c_1$	5.01×10^{-5} m^{-1}
Group velocity of the pump wave, $c_g = \sqrt{3}c_1/2$	2.11 m s^{-1}
Energy flux, $\rho_0 J = \rho_0\sqrt{3}a^2 \int_0^H \rho_1^2\,\mathrm{d}z/c_1$	0.78 kW m^{-1}
Pump strength, $\upsilon = ak^2/2f_0 = 3f_0a/2c_1^2$	1.788×10^{-6} s^{-1}
Maximum growth rate, $\gamma_{max} = \upsilon/2$	1/(13 days)
PSI wavenumbers, (k_1, l_1) and (k_2, l_2)	$(2k, 0)$ and $(-k, 0)$

TABLE 1. Parameter values used in the computations. We take $\omega = 2f_0$ and compute the pump wavenumber, k, from the dispersion relation $\omega^2 = f_0^2 + c_1^2k^2$. The resulting wavelength, $2\pi/k$, is 125 km. Observations made by Rainville & Pinkel (2006) as part of the HOME experiment indicate a northward flux of tidal energy of 1.7 kW m^{-1}. To match these observations roughly we should increase a by about $\sqrt{2}$, which would increase the maximum growth rate to 1/ (9 days).

rate is achieved for modes with vertical structure of moderate scale. On the other hand, with smaller σ, the growth rate converges much more slowly, but it does seem to converge.

A numerical demonstration of convergence is not totally convincing and so some analytic support is reassuring. We begin by noting that the most-unstable eigenfunction shown in figure 9 is strongly localized to the base of the mixed layer

https://doi.org/10.1017/S0022112008001742 Published online by Cambridge University Press

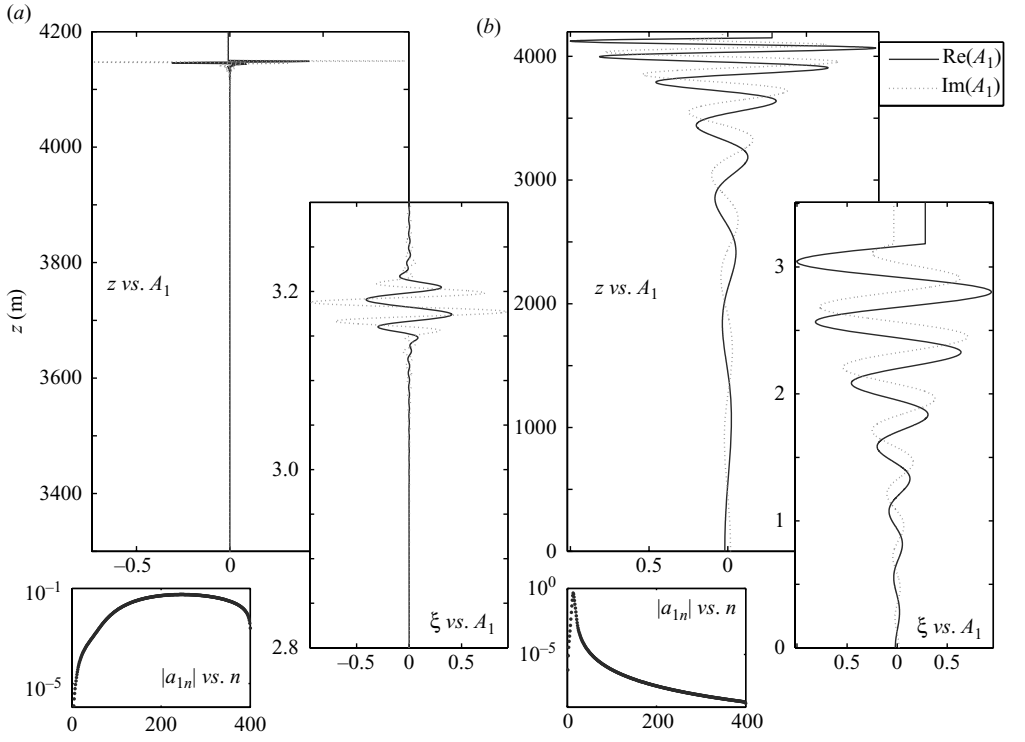


FIGURE 9. Real and imaginary parts of $A_1(z,t)$, for the most unstable modes with (*a*) perfect resonance $\sigma = 0$ and (*b*) slight de-tuning $\sigma = 2\upsilon$. In both cases $k_1 = 2k$, $k_2 = -k$ and $l_1 = l_2 = 0$. The large insets display the eigenfunctions against the stretched coordinate $\xi(z)$ in (B 7). The small lower insets shows the coefficients obtained by solving (5.11) i.e., $|a_{1n}|$ against n. In the left panel the solution is dominated by the high modes with the smallest scales and the solution is concentrated at the base of the mixed layer (note the expanded vertical scales).

where $p_1(z) \approx 1$; and because of the violent oscillations in the eigenfunction, terms in (5.5) involving the second-order differential operator L are large. Thus, we expect that (5.5) reduces to

$$\left(s - \tfrac{1}{2}\mathrm{i}\sigma\right)A_1 + \tfrac{1}{2}\mathrm{i}\upsilon A_2 \approx 0, \tag{5.13a}$$

$$\left(s + \tfrac{1}{2}\mathrm{i}\sigma\right)A_2 - \tfrac{1}{2}\mathrm{i}\upsilon A_1 \approx 0, \tag{5.13b}$$

giving

$$s \approx \tfrac{1}{2}\sqrt{\upsilon^2 - \sigma^2}\,. \tag{5.14}$$

Indeed, the first and largest bump in the growth rate shown rate in figure 10 falls on top of this estimate (see the dotted curve), and with $\sigma = 0$ we recover (5.12) from (5.14). The curve-like structures evident in figure 8 for higher truncations, $\mathcal{N}$, can be interpreted as the extension of this formula to different vertical levels, with z parameterizing the curves through the dependence of $p_1(z)$. The rightmost extension of the curves occurs at the base of the mixed layer where $p_1(z) \to 1$.

For larger σ, the unstable modes are no longer localized to the base of the mixed layer, and the smaller bumps in figure 10 are not explained by a simple approximation like (5.14). Instead, the smaller bumps can be rationalized as follows. The eigenvalue

https://doi.org/10.1017/S0022112008001742 Published online by Cambridge University Press

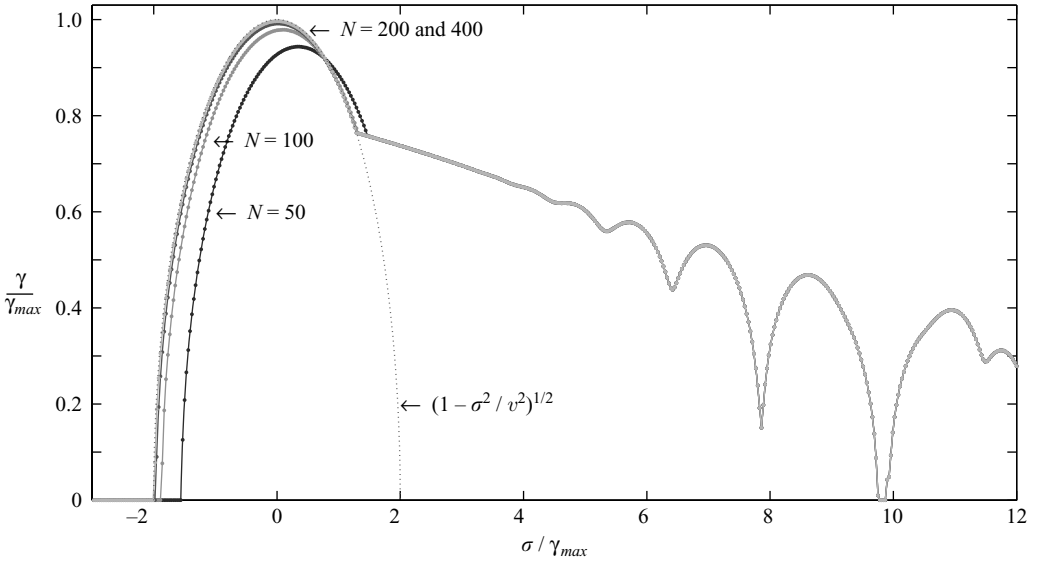


FIGURE 10. Maximum growth rates against σ for $l_1 = l_2 = 0$, $k_1 = 2k$ and $k_2 = -k$ and with indicated truncations ($\mathcal{N} = 50$, 100, 200 and 400) of (5.11). By $\mathcal{N} = 400$, the growth rate has converged. The dotted curve shows the analytic result (5.14). The instability disappears for sufficiently large, negative de-tuning (i.e. $\sigma < -\upsilon$), and a curious bumpy structure emerges in the growth rate for larger positive de-tuning.

problem can be rewritten as

$$\left(s + \mathrm{i}\omega_n^{(1)}\right) a_{1n} = -\tfrac{1}{2}\mathrm{i}\upsilon \sum_q M_{nq} a_{2q}, \tag{5.15a}$$

$$\left(s - \mathrm{i}\omega_n^{(2)}\right) a_{2n} = \tfrac{1}{2}\mathrm{i}\upsilon \sum_q M_{nq} a_{1q}, \tag{5.15b}$$

where $\omega_n^{(j)}$ is defined in (5.10). For $\sigma \gg \upsilon$ and $K_j^2 c_n^2 / f_0 \gg \upsilon$, the two relations in (5.15) are dominated by the left-hand sides. Thus, we have crude approximations to the eigenvalues

$$s \sim -\mathrm{i}\omega_I^{(1)} \qquad \text{or} \qquad s \sim \mathrm{i}\omega_J^{(2)}, \tag{5.16}$$

for some integers I and J. When satisfied separately, either condition above generates an imaginary eigenvalue. For example, the first condition leads to an eigenvector which is dominated by the component, a_{1I}, with the other components all small. In this case, the eigenvalue is imaginary and there is no growth. However, if both conditions in (5.16) are satisfied simultaneously, i.e. if

$$\omega_I^{(1)} + \omega_J^{(2)} \approx 0, \tag{5.17}$$

then the eigenvector is a mixture of a_{1I} and a_{2J}. In this resonant case, the eigenvalue is determined by solving

$$\left(s + \mathrm{i}\omega_I^{(1)}\right)\left(s - \mathrm{i}\omega_J^{(2)}\right) \approx \tfrac{1}{4}\upsilon^2 M_{IJ} M_{JI}, \tag{5.18}$$

giving

$$s = \tfrac{1}{2}\mathrm{i}\left(\omega_J^{(2)} - \omega_I^{(1)}\right) \pm \tfrac{1}{2}\sqrt{\upsilon^2 M_{IJ} M_{JI} - \left(\omega_J^{(2)} + \omega_I^{(1)}\right)^2}. \tag{5.19}$$

https://doi.org/10.1017/S0022112008001742 Published online by Cambridge University Press

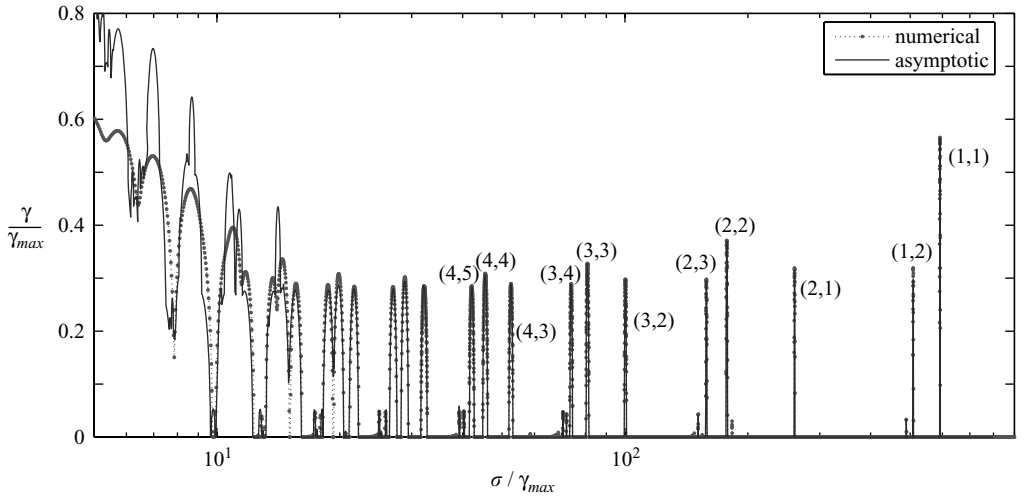


FIGURE 11. Growth rates for large σ, showing numerical computations (dots) and the superposition obtained from (5.19) (solid lines). The superposition includes the triad resonances, (I, I), $(I, I \pm 1)$, $(I, I \pm 2)$ and $(I, I \pm 3)$, with $I = 1, 2, \ldots, 12$. The dominant peaks for larger σ are identified by their respective values of the pairs, (I, J). The parameter settings are as in figure 10.

The expression for s above is similar in structure to our earlier result for the PSI growth rate in (4.17). The resonance condition in (5.17) predicts an unstable mode coupling near

$$\sigma_{IJ} = \frac{k_1^2 c_I^2 + k_2^2 c_J^2}{2 f_0}. \tag{5.20}$$

The physical interpretation is that triad resonance occurs between discrete vertical modes $p_I(z)$ and $p_J(z)$ in a frequency band surrounding σ_{IJ} in (5.20). Since the c_n decrease with increasing n, the resonance with the largest possible σ_{IJ} is $I = J = 1$, giving $\sigma_{11} = (k_1^2 + k_2^2)c_1^2/f_0$. De-tuning above the band centred on σ_{11} completely eliminates PSI. In other words, the range of unstable de-tuning parameters is given roughly by

$$-\upsilon < \sigma < \left(k_1^2 + k_2^2\right) c_1^2 / f_0. \tag{5.21}$$

The growth rates for the most unstable triad resonances, as predicted by (5.19) and superposed, are shown in figure 11. For comparison, this figure also displays the continuation of the numerical results in figure 10 to higher values of the de-tuning parameter σ. Because the matrix, M_{IJ}, is dominated by its three leading diagonals, the strongest triads are given by the pairs, $(I, J) = (I, I)$ and $(I, I \pm 1)$, as shown by the figure. When σ becomes smaller, the bands of unstable triads overlap to form a continuous increasing growth-rate curve. However, the approximation (5.19) also becomes less accurate and overestimates the growth rates. Instead, for small σ, the alternative approximation (5.14) is very accurate. In this limit, with small de-tuning, the mode-one wavetrain is pumping a vertical continuum (rather than discrete resonant triads) of near-inertial oscillations.

https://doi.org/10.1017/S0022112008001742 Published online by Cambridge University Press

6. Conclusion and discussion

The method of multiple time scales has been used to obtain an amplitude equation (3.45) describing the evolution of near-inertial disturbances. An important new ingredient in this reduced description of the near-inertial peak is an energy source produced by the parametric subharmonic instability of a 'pump wave' with frequency close to $2f_0$. The term $\Upsilon LA^*/2$ in (3.45) is a general expression for this source of near-inertial energy. It is notable that neither the horizontal divergence, $U_x + V_y$, nor the vertical vorticity, $V_x - U_y$, of the pump appear in the expression for Υ in (3.47). Moreover, although vertical advection of the near-inertial fields by the pump wave is the strongest nonlinearity, vertical advection does not produce energy transfer. (Vertical advection appears at first order in the expansion, i.e. in (3.34). The resonant terms resulting in PSI appear at second order, i.e. in (3.43).) Instead, for near-inertial PSI, the physical argument of § 2 identifies the $2f_0$-spectral content of the horizontal strain, $U_x - V_y$ and $V_x + U_y$, as the key driver of PSI. In this sense, PSI is misnamed: the instability is not due to the periodic variation of a parameter (e.g. N^2) in the dispersion relation of internal gravity waves.

As an application of (3.45), in § 4 we examine the subharmonic instability of an infinite-plane internal gravity wave, with frequency close to $2f_0$; we obtain an analytic expression for the growth rate of near-inertial PSI in (4.18). Order-of-magnitude estimates using oceanic parameter values indicate that the e-folding time scale of near-inertial PSI is ten days or less. In § 5, we use a more realistic model of the pump wave based on a surface intensified buoyancy frequency. Thus, the mode-one vertical structure of the pump wave has largest amplitude at the base of the mixed layer, and consequently the unstable near-inertial disturbance is also localized just beneath the base of the mixed layer. In this situation we again find that γ_{max} in (4.19) applies to the fastest growing near-inertial disturbances.

The linear stability calculations of §§ 4 and 5 show that if the de-tuning is close to resonant then the fastest growing waves have large (or infinite) vertical wavenumbers. Additional physical factors, such as scale-selective dissipation, non-zero β, or secondary instabilities, must become important. In our numerical solutions of the two-dimensional Boussinesq equations, the hyperdissipation provides this regularization. A main open issue is which of the mechanisms above is important in the geophysical context? We speculate that $\beta \neq 0$ might significantly affect the high-wavenumber behaviour of near-inertial PSI: the continuous variation of the Coriolis parameter with latitude ensures that near-resonant PSI occurs only in a strip surrounding the resonant latitude (which is 28.8° for an M_2 pump wave). Rough estimates show that the width of this strip is comparable to a single wavelength of the internal tidal wave, and the implications of this observation are now being investigated.

We thank Chris Garrett, Kraig Winters, Eric Kunze, Jen MacKinnon and Visweswaran Nageswaran for discussions related to this work. This work was supported by the National Science Foundation by grant number OCE07-26320.

Appendix A. The numerical model

We solve the two-dimensional nonlinear non-hydrostatic Boussinesq equations in the (x, z)-plane using the streamfunction formulation $(u, w) = (-\psi_z, \psi_x)$. The

https://doi.org/10.1017/S0022112008001742 Published online by Cambridge University Press

equations of motion are

$$\nabla^2\psi_t + J(\psi, \nabla^2\psi) + f_0 v_z = b_x - \mathscr{D}(\zeta), \tag{A 1}$$

$$v_t + J(\psi, v) + f_0 u = -\mathscr{D}(v), \tag{A 2}$$

$$b_t + J(\psi, b) + N^2 w = -\mathscr{D}(b), \tag{A 3}$$

where $\nabla^2 = \partial_x^2 + \partial_z^2$ and $J(p, q) = p_x q_z - p_z q_x$ is the Jacobian. $\mathscr{D}$ is a hyperviscous operator defined by considering a domain of size $L_x \times L_z$, with grid spacing Δx and Δz in the horizontal and vertical direction, respectively:

$$\mathscr{D}(\phi) \equiv \nu \left[\left(\frac{\Delta x}{\Delta z} \right)^2 \partial_x^2 + \partial_z^2 \right]^4 \phi, \tag{A 4}$$

where ν is the hyperviscosity. In our simulations $\Delta x \gg \Delta z$: the numerical resolution is greater in the vertical direction because $L_x \gg L_z$. The anisotropic hyperdiffusion in (A 4) prevents aliasing in both directions. A similar procedure is used by Bouruet-Aubertot *et al.* (1995) in their numerical simulations of non-rotating PSI.

Typical values of ν are $10^{-15}\,\mathrm{km}^8\,\mathrm{h}^{-1} \leqslant \nu \leqslant 5 \times 10^{-15}\,\mathrm{km}^8\,\mathrm{h}^{-1}$. We usually used $N_x = 256$ modes in the x-direction and $N_z = 512$ modes in the z-direction so that the solution is represented as

$$\psi(x, z, t) = \sum_{p=-N_x/2}^{N_x/2} \sum_{q=-N_z/2}^{N_z/2} \hat{\psi}_{pq}(t) \exp\left(\mathrm{i}\frac{2\pi p x}{L_x} + \mathrm{i}\frac{2\pi q z}{L_z} \right), \tag{A 5}$$

with $\hat{\psi}_{pq} = \hat{\psi}^*_{-p-q}$. In simulations, such as the example in figure 1, the initial condition is the plane-wave in (4.1) with $k = 2\pi/L_x$ and $m = 2\pi/L_z$, plus small noise. That is, the initial condition projects mainly onto the modes $(p, q) = \pm(1, 1)$ in (A 5).

To define the growth of the perturbation we write

$$\psi = [\hat{\psi}_{11}(t) \exp(\mathrm{i}kx + \mathrm{i}mz) + \text{c.c.}] + \psi', \tag{A 6}$$

with an analogous decomposition for b and v. The energy, $e = \langle |\nabla\psi|^2 + v^2 + N^{-2}b^2 \rangle / 2$, is decomposed as the energy in the modes $(p, q) = \pm(1, 1)$, plus the disturbance energy e':

$$e = e_{11}(t) + e'(t). \tag{A 7}$$

During the linear phase, corresponding to the straight-line portion of the curves in figure 3, e is constant and $e'(t)$ grows exponentially from a very small initial level. Thus, as an index of the disturbance amplitude, in figure 3 we use the normalized disturbance energy

$$E' \equiv e'/e. \tag{A 8}$$

Figure 3 shows that PSI eventually saturates when $E' = O(1)$, indicating that the modes with $(p, q) = \pm(1, 1)$ have lost a substantial fraction of their initial energy to near-inertial oscillations.

Appendix B. Gill's normal modes

Gill (1984) proposed a realistic model of the oceanic stratification which has the advantage that convenient expressions for the eigenmodes are available. Gill's

https://doi.org/10.1017/S0022112008001742 Published online by Cambridge University Press

buoyancy frequency is:

$$N(z) = \begin{cases} s/(z_0 - z), & 0 \leqslant z \leqslant H - H_{mix}, \\ 0, & H - H_{mix} < z \leqslant H, \end{cases} \tag{B 1}$$

and the vertical modes satisfy

$$Lp_n \equiv \frac{\mathrm{d}}{\mathrm{d}z}\left(\frac{f_0^2}{N^2}\frac{\mathrm{d}p_n}{\mathrm{d}z}\right) = -\frac{f_0^2}{c_n^2}p_n, \qquad p_n'(0) = p_n'(H) = 0\,, \tag{B 2}$$

with normalization $p_n(H) = 1$. The barotropic mode ($n = 0$) corresponds to the eigenvalue $f_0^2/c_0^2 = 0$ and the eigenfunction $p_0(z) = 1$.

The eigenmodes are

$$p_n(z) = \begin{cases} \mathrm{e}^{(\xi - \xi_T)/2}\dfrac{2m_n \cos m_n\xi - \sin m_n\xi}{2m_n \cos m_n\xi_T - \sin m_n\xi_T}, & 0 \leqslant \xi \leqslant \xi_T, \\ 1, & \xi_T < \xi. \end{cases} \tag{B 3}$$

Above, m_n is defined by

$$c_n^2 \equiv \frac{4s^2}{4m_n^2 + 1}\,; \tag{B 4}$$

the stretched coordinate is

$$\xi \equiv -\log\left(1 - \frac{z}{z_0}\right), \tag{B 5}$$

and

$$\xi_T \equiv -\ln\left[1 - \frac{H - H_{mix}}{z_0}\right]. \tag{B 6}$$

The eigencondition, determining c_n and m_n, is

$$\sin m_n\xi_T + \epsilon m_n \cos m_n\xi_T = 0, \tag{B 7}$$

where

$$\epsilon \equiv \left(\frac{1}{2} + \frac{z_0 - H}{H_{mix}}\right)^{-1}. \tag{B 8}$$

The eigenfunctions satisfy the orthogonality condition:

$$\int_0^H p_k(z)p_l(z)\,\mathrm{d}z = \frac{H_{mix}\left(4m_k^2 + 1\right)\left[\epsilon + \xi_T\left(1 + \epsilon^2 m_k^2\right)\right]}{4\epsilon(2 + \epsilon)m_k^2}\delta_{kl}. \tag{B 9}$$

The integral over $p_1(z)p_n(z)p_{n'}(z)$ in (5.8) can also be evaluated analytically which is how we computed the matrix $M_{nn'}$ in § 5. However, the expression for $M_{nn'}$ is unwieldy and so we omit it.

REFERENCES

Benielli, D. & Sommeria, J. 1998 Excitation and breaking of internal gravity waves by parametric instability. *J. Fluid Mech.* **374**, 117–144.

Bouruet-Aubertot, P., Sommeria, J. & Staquet, C. 1995 Breaking of standing internal gravity waves through two-dimensional instabilities. *J. Fluid Mech.* **285**, 265–301.

Drazin, P. G. 1977 On the instability of an internal gravity wave. *Proc. R. Soc. Lond.* A **356**, 411–432.

Garrett, C. J. R. & St Laurent, L. 2002 Aspects of deep ocean mixing. *J. Oceanogr.* **58**, 11–24.

https://doi.org/10.1017/S0022112008001742 Published online by Cambridge University Press

Gerkema, T., Staquet, C. & Bouruet-Aubertot, P. 2006 Decay of semi-diurnal internal-tide beams due to subharmonic resonance. *Geophys. Res. Lett*. **33**, L08604, doi 10.1029/2005GL025105.

Gill, A. E. 1984 On the behavior of internal waves in the wakes of storms. *J. Phys. Oceanogr*. **14**, 1129–1151.

Hibiya, T., Nagasawa, M. & Niwa, Y. 2002 Nonlinear energy transfer within the oceanic internal wave spectrum at mid and high latitudes *J. Geophys. Res.* **103** C9, doi 10.1029/98JC01362.

Klein, P. & Llewellyn Smith, S. L. 2001 Horizontal dispersion of near-inertial oscillations in a turbulent mesoscale eddy field. *J. Mar. Res.* **59**, 697–723.

Klein, P., Llewellyn Smith, S. L. & Lapeyre, G. 2004 Organization of near-inertial energy by an eddy field. *Q. J. R. Met. Soc*. **130**, 1153–1166.

Klostermeyer, J. 1991 Two- and three-dimensional parametric instabilities in finite-amplitude internal gravity waves. *Geophys. Astrophys. Fluid Dyn*. **61**, 1–25.

Kunze, E. 1985 Near inertial wave propagation in geostrophic shear. *J. Phys. Oceanogr*. **15**, 544–565.

McComas, C. H. & Bretherton, F. P. 1977 Resonant interactions of oceanic internal waves. *J. Geophys. Res.* **82**, 1397–1412.

MacKinnon, J. A. & Winters, K. B. 2005 Subtropical catastrophe: significant energy loss of low-mode tidal energy at 28.9°. *Geophys. Res. Lett*. **32**, L15605, doi 10.1029/2005GL023376.

MacKinnon, J. A. & Winters, K. B. 2008 Tidal mixing hotspots governed by rapid parametric subharmonic instability. *J. Phys. Oceanogr*. (submitted).

Mied, R. P. 1976 The occurrence of parametric instabilities in finite amplitude internal gravity waves. *J. Fluid Mech*. **78**, 763–784.

Müller, P., Holloway, G., Henyey, F. & Pomphrey, N. 1986 Nonlinear interactions among internal gravity waves. *Rev. Geophys*. **24**, 493–536.

Nagasawa, M., Niwa, Y. & Hibiya, T. 2000 Spatial and temporal distribution of the wind-induced internal wave energy available for deep water mixing in the North Pacific *J. Geophys. Res.* **105**, 13 933–13 943.

Olbers, D. & Pomphrey, N. 1981 Disqualifying two candidates for the energy balance of oceanic internal waves. *J. Phys. Oceanogr*. **11**, 1423–1425.

Rainville, L. & Pinkel, R. 2006 Baroclinic energy flux at the Hawaiian Ridge: observations from the R/P FLIP. *J. Phys. Oceanogr*. **36**, 1104–1122.

Reznik, G. M., Zeitlin, V. & Ben Jelloul, M. 2001 Nonlinear theory of geostrophic adjustment. Part 1. Rotating shallow-water model *J. Fluid Mech*. **445**, 93–120.

Simmons, H. L. 2008 Spectral modification and geographic redistribution of the semi-diurnal internal tide. *Ocean Modelling* **21**, 126–128.

Weller, R. A. 1982 The relation of near-inertial motions observed in the mixed layer during the JASIN (1978) experiment to the local wind stress and to the quasi-geostrophic flow field. *J. Phys. Oceanogr*. **12**, 1122–1136.

Young, W. R. & Ben Jelloul, M. 1997 Propagation of near-inertial oscillations through a geostophic flow. *J. Mar. Res*. **55**, 735–766.

https://doi.org/10.1017/S0022112008001742 Published online by Cambridge University Press